

# Minimal Visual Occlusion Redundancy Resolution of Continuum Robots in Confined Spaces

Nima Sarli<sup>1,2</sup>, Nabil Simaan<sup>1,2,♠</sup>

**Abstract**—Minimally invasive surgery in confined spaces often requires the coordinated use of endoscopes and surgical tools while minimizing visual occlusions. In a robotic system such visual occlusion avoidance has to be achieved autonomously while keeping the surgical end effector as close as possible to the center of the field of view of the endoscope. This paper presents an investigation of use of redundancy resolution to solve the problem of visual occlusion. Specifically, the paper addresses hard cases where a continuum robot or an ablation catheter emanate from a narrow access channel containing an endoscope. A redundancy resolution method accounting for the kinematics of the continuum robot and allowing for rotation of an angle lens endoscope is presented. A potential field method is used to guide all portions of the continuum arm outside of the visualization cone of the endoscope and a gradient descent method is used to guide the rotation of the endoscope to keep the end effector as close as possible to the center of the visual field of the endoscope. A simulation case study demonstrates the utility of our method using a recently designed transurethral bladder cancer surgery system as a demonstration platform. Although the context of the problem is bladder surgery utilizing a continuum robot, the method can be generalized to any redundant robot that requires to accomplish a task with minimal visual occlusion.

**Index Terms**—continuum robot, redundancy resolution, visual occlusion, camera field of view

## I. INTRODUCTION

The advent of less invasive robotic systems for minimally invasive surgery (MIS) in deep surgical fields presents new challenges for robot designers and users. For example, robotic systems for operating in deep and narrow spaces (e.g. trans-oral minimally invasive surgery of the upper airways, transurethral endoscopic, transnasal-endoscopic, middle-ear endoscopic and trans-anal endoscopic surgeries) present difficulties in visualization as well as in dexterous manipulation. Such difficulties stem from the fact that, in such systems, often the endoscope axis and the axis of the surgical access channel lie almost parallel to each other and with a small offset. As a result, the visual field of an endoscope can be easily occluded when the tools move in front of it. During manual MIS, surgeons can use angled lens endoscopes and can rotate the lens to shift the field of view (FOV) to follow the tool tip. During robotic surgery - and especially when using continuum robots for added dexterity - this problem is exacerbated because the body of the continuum robot

often emanates from the access channel in close proximity to the tip of the endoscope. This creates severe problems of visual occlusion when the continuum robot is controlled using native resolved rates control.

This work is motivated by recent experiences we had when deploying our trans-urethral resection of bladder tumors (TURBT) system. Early ex-vivo concepts of this system were reported in [1], [2]. Our recent TURBT system including a custom surgical access channel (called a resectoscope), a *multi-backbone continuum robot* (MBCR), and a holmium laser for resection was first presented in [3]. This system addresses the clinical needs for preliminary testing in pig experiments. However, initial evaluation has revealed the difficulties of visualization as demonstrated in Fig. 1-(a,b). In addition to the limited depth perception when using endoscopic surgery (e.g. as reported in [4]), other critical difficulties hindering successful use of this system in an animal trial were visual occlusion of the robot tip by its own body and the narrow visualization workspace as observed from an endoscope.

To solve these problems, we have drawn inspiration from manual endoscopic surgery where surgeons rely on the rotation of an angled lens endoscope to help maintain visualization of the end effector. Though we could have considered the use of a steerable endoscope to help solve the visual occlusion problem, we have elected to treat the case of a straight endoscope because 1) it is more restrictive, 2) the cost of a straight Hopkins rod endoscope is a fraction of the cost of a steerable endoscope, 3) sterilizable steerable endoscopes with diameters fitting our 3 mm endoscopic access channel have very narrow FOV and relatively short focal range.

To address this need, this paper investigates the use of redundancy resolution to minimize visual occlusion while assuming that an angled-lens endoscope can be actively rotated to shift the direction of the FOV. We also assume that a computer algorithm for visually rotating re-centering of the camera view can be implemented in future applications of our method so that the user does not get disoriented when tele-manipulating such robots.

Works relevant to this paper are in the area of obstacle avoidance for continuum robots and control of camera position for surgical applications in order to maintain the end effector in the FOV. Li and Xiao proposed a method for sampling the configuration space of continuum robots to produce motion plans allowing these robots to operate within constrained environments [5]. Reiter and Allen [6] who presented automatic tracking of the arms of the IREP single

\* This research was supported by NIH grant R21EB015623-01A1

<sup>1</sup>Department of Mechanical Engineering, Vanderbilt University, Nashville, TN 37240, USA, {nima.sarli, nabil.simaan}@vanderbilt.edu.

<sup>2</sup>Vanderbilt Institute in Surgical Engineering (VISE), Nashville, Tennessee, USA

♠ Corresponding author

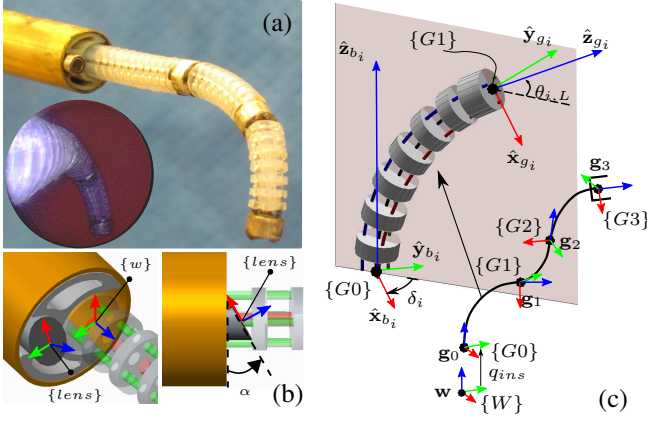


Fig. 1: (a) TURBT robot distal section, inset shows camera view, (b) External sheath tip, (c) Multibackbone continuum robot schematic

port access system. This work however did not consider the problem of how to control the continuum arms of the robot to minimize visual occlusion. Baumann et al. [7] applied a modified probabilistic roadmap method (PRM) to penalize the motions of an articulated serial robot that block the line of sight of an eye-in-hand camera while reaching the visual target [8], [9]. Leonard et al. used PRM and a dynamic collision checking algorithm to plan occlusion-free motions for industrial robots. They modeled the FOV of an eye-to-hand (stationary) camera as a quadtree of frustums and applied adaptive dynamic collision checking algorithms to avoid colliding pre-selected pixels in the view frustum of the camera [10]. In the area of visual servoing, preservation of visibility is of significant importance as the loss of visual information jeopardizes the stability and/or performance of feedback control. Visual target loss occurs due to the robot self-occlusion or the target departure from FOV. Therefore, designing algorithms and controllers that guarantee visible robot configurations has been a critical problem that was addressed in multiple studies [11–15]. Most if not all such work in the visual servoing field rely on the image space information for their algorithms. More importantly, none of the prior literature utilizes the kinematic redundancy of the robot to address occlusion minimization.

The main contribution of this study is in utilizing the robot kinematic redundancy to minimize the FOV occlusion. To achieve this, a modified artificial potential field approach in path planning is applied to drive the robot body outside the FOV while achieving the main tracking task. The proposed algorithm can be directly applied to any redundant robot performing a task under the surveillance of a camera. Moreover, it does not require the camera intrinsic parameters calibration since it does not use image space information.

The article is structured as follows. In section II, the kinematics of MBCR is briefly explained. Section III defines the problem. In section IV, the solution approach is delineated in details. This includes descriptions of the potential function derivation, a suitable force field definition, the redundancy resolution framework and a visual occlusion index. Simulation results and discussions are brought in

section V. Finally the article is concluded with a summary in section VI.

## II. KINEMATICS OF MBCR

The kinematics of multi-segment MBCR was explained in details in [16–18]. For completeness on this work, we hereby present a summary of the kinematics of these robots.

Figure (1)-b shows a schematic of a three-segment MBCR. The configuration of the  $j^{th}$  segment ( $j = 1, 2, 3$ ) is represented by  $\psi_j = [\theta_{j,L}, \delta_j]^T$  where  $\theta_{j,L}$  is the bending angle and  $\delta_j$  is the bending plane angle as shown in Fig. (1-c). The continuum robot can also control its insertion  $q_{ins}$  relative to the resectoscope. We will use therefore  $\tilde{\psi} = [\psi_1^T, \psi_2^T, \psi_3^T, q_{ins}]^T \in \mathbb{R}^{7 \times 1}$  as a configuration vector and  $\xi$  as the end-effector twist<sup>1</sup>. Using these definitions, the instantaneous kinematics of the MBCR is given by:

$$\mathbf{J}_{x\tilde{\psi}} \dot{\tilde{\psi}} = \dot{\xi} \quad (1)$$

where the instantaneous inverse kinematics Jacobian  $\mathbf{J}_{x\tilde{\psi}} \in \mathbb{R}^{6 \times 7}$ , is expressed as a function of the instantaneous Jacobians of each continuum segment as:

$$\mathbf{J}_{x\tilde{\psi}} = [\mathbf{S}_1 \mathbf{J}_{x\psi_1}, \mathbf{S}_2 \mathbf{J}_{x\psi_2}, \mathbf{S}_3 \mathbf{J}_{x\psi_3}, \mathbf{e}_4] \quad (2)$$

where  $\mathbf{J}_{x\psi_j}$  represents the Jacobian of the  $j^{th}$  segment MBCR. This Jacobian was derived in ([16], [17]):

$$\mathbf{J}_{x\psi_j} = \begin{bmatrix} l_j c_{\delta_j} \chi_1 & -l_j s_{\delta_j} \chi_3 \\ -l_j s_{\delta_j} \chi_1 & -l_j c_{\delta_j} \chi_3 \\ l_j \chi_2 & 0 \\ -s_{\delta_j} & c_{\delta_j} c_{\theta_{j,L}} \\ -c_{\delta_j} & -s_{\delta_j} c_{\theta_{j,L}} \\ 0 & -1 + s_{\theta_{j,L}} \end{bmatrix} \quad (3)$$

$$\chi_1 \triangleq \frac{(\theta_{j,L} - \pi/2) c_{\theta_{j,L}} - s_{\theta_{j,L}} + 1}{(\theta_{j,L} - \pi/2)^2},$$

$$\chi_2 \triangleq \frac{(\theta_{j,L} - \pi/2) s_{\theta_{j,L}} + c_{\theta_{j,L}}}{(\theta_{j,L} - \pi/2)^2},$$

$$\chi_3 \triangleq \frac{s_{\theta_{j,L}} - 1}{(\theta_{j,L} - \pi/2)}$$

where  $s. \triangleq \sin(.), c. \triangleq \cos(.), \mathbf{e}_4 = [0, 0, 1, 0, 0, 0]^T$ .  $l_j$  is the length of the  $j^{th}$  segment.  $\mathbf{S}_j, j = 1, 2, 3$  are twist transformation matrices given by:

$$\mathbf{S}_j = \begin{bmatrix} {}^w\mathbf{R}_{j-1} & ({}^w\mathbf{g}_j - {}^w\mathbf{g}_3)^\wedge \\ \mathbf{0}_3 & {}^w\mathbf{R}_{j-1} \end{bmatrix}, \quad j = 1, 2, 3 \quad (4)$$

where  ${}^w\mathbf{R}_{j-1}$  is the rotation matrix from the base of the  $j^{th}$  segment to the world frame  $\{W\}$ <sup>2</sup>. This rotation is given by:

$${}^w\mathbf{R}_j = \prod_{i=1}^j {}^w\mathbf{R}_0^{i-1} \mathbf{R}_i, \quad j = 1, 2, 3 \quad (5)$$

<sup>1</sup>we use the twist notation in which linear velocity precedes angular velocity

<sup>2</sup>we will use  ${}^j\mathbf{x}$  to designate vector  $\mathbf{x}$  expressed in frame  $\{j\}$  and  ${}^j\mathbf{R}_i$  to designate the rotation matrix relating frame  $\{i\}$  to frame  $\{j\}$

and  ${}^{i-1}\mathbf{R}_i$  is the direct orientation kinematics of the  $i^{th}$  segment. Referring to Fig. 1-(c) and using  $\hat{\mathbf{e}}_i$  as the  $i^{th}$  canonical base vector of  $\mathbb{R}^3$  we obtain:

$${}^{i-1}\mathbf{R}_i = e^{-\delta_i \hat{\mathbf{e}}_3^\wedge} e^{(\pi/2 - \theta_{i,L}) \hat{\mathbf{e}}_2^\wedge} e^{\delta_i \hat{\mathbf{e}}_3^\wedge} \quad (6)$$

The  $(\cdot)^\wedge$  operator in Eqs. (4, 6) returns the cross-product matrix of vector  $(\cdot)$ .  ${}^w\mathbf{g}_j$  is the position of the end disk of the  $j^{th}$  segment (Fig. (1)-c). This vector is given by:

$${}^w\mathbf{g}_j = \sum_{i=1}^j {}^w\mathbf{R}_{i-1} {}^{i-1}\mathbf{g}_{i/b_i}, \quad j = 1, 2, 3 \quad (7)$$

where  ${}^{i-1}\mathbf{g}_{i/b_i} = ({}^{i-1}\mathbf{g}_i - {}^{i-1}\mathbf{g}_{i-1})$  is the position of the end disk of the  $i^{th}$  segment with respect to its base, expressed in frame  $\{i-1\}$ . Using [16],  ${}^{i-1}\mathbf{g}_{i/b_i}$  is:

$${}^{i-1}\mathbf{g}_{i/b_i} = \frac{l_i}{\theta_{i,L} - \pi/2} \begin{bmatrix} c\delta_i(s_{\theta_{i,L}} - 1) \\ -s\delta_i(s_{\theta_{i,L}} - 1) \\ -c\theta_{i,L} \end{bmatrix} \quad (8)$$

### III. PROBLEM STATEMENT AND ASSUMPTIONS

Based on Fig. (1)-b, the world coordinate frame  $\{w\}$  is at the center of MBCR working channel with the z-axis along the axis of the resectoscope sheath (yellow tube). The lens coordinate frame  $\{lens\}$  is attached to the endoscope tip lens such that its z-axis is normal to the lens. For simplicity of presentation, we assume that there are no motion constraints on the MBCR (e.g. induced by the external sheath). Such constraints may be dealt with as in [19].

The problem we wish to solve is to command the end-effector of the MBCR to track a desired twist  $\dot{\xi}$  while using redundancy to minimize visual occlusion. We assume that occlusion can be minimized by applying a proper force on the MBCR so that its resultant equilibrium configuration causes minimal occlusion. This static equilibrium is sought according to the virtual work principle by minimizing the potential energy of the system (The mechanical energy of the MBCR including elastic potential and an artificial potential due to visual occlusion) subject to the kinematics of MBCR. Though a task priority redundancy resolution approach as presented in [20] is possible, we pursue a redundancy resolution using gradient projection for the simplicity:

$$\begin{aligned} &\text{Minimize} \quad \Pi \\ &\text{subject to} \quad \mathbf{J}_{x\tilde{\psi}} \dot{\tilde{\psi}} = \dot{\xi} \end{aligned} \quad (9)$$

### IV. SOLUTION METHOD

In motion planning by artificial potentials, the potential function  $U_r$  refers to an artificial *repulsive* potential that prevents *psp*'s (point subject to potential) to collide with the obstacles in the environment. This repulsive potential is added to *attractive* potential  $U_a$  so the robot can reach the goal by attraction toward it while avoiding the obstacles [21], [22]. The repulsive potential is chosen such that the rendered force on the robot vanishes after a certain *distance of influence* and approaches infinity as the *psp* approaches the obstacle. If *psp*'s are selected appropriately, this ensures the robot never collides with the obstacles while satisfying

the main task of tracking<sup>3</sup>. In this study, a similar approach is adopted in that a potential function is minimized locally, however there are key differences that are outlined here.

The first difference is in the choice of the potential function. In our study, this function has contributions from an artificial repulsive field as well as the gradient of the strain energy of the continuum robot. This potential function denoted hereafter  $\Pi$  stems from the application of principle of virtual work as will be shown. Also, the repulsive field generates a force that is designed to push the *psp*'s outside the FOV. These forces do not grow infinite as the *psp*'s collide with the FOV cone as that is a requisite to achieve the main task, rather they grow larger at an adjustable rate as the *psp*'s move toward the inside of FOV and they diminish as the *psp*'s move outside the FOV and the distance of influence.

A second difference is that no attractive potential is used to fulfil the main task. Instead, we use pseudo-inverse with gradient projection to resolve the redundancy at velocity level for the purpose of the real-time control while minimizing the occlusion.

#### A. Potential Function

The principle of virtual work states that the mechanical energy  $\Pi$  is stationary at an equilibrium point (i.e.  $\delta\Pi \triangleq \delta(E - W) = 0$  where  $E$  and  $W$  represent the potential (elastic) energy and work of external force respectively. In our problem, the elastic energy  $E$  includes the bending strain energy of all the backbones. The gravitational and the axial strain energy of the backbones can be neglected for robots of small size as ours [24]. Therefore, the elastic energy is expressed as in [17]:

$$E = \sum_{i=1}^3 (\pi/2 - \theta_{i,L})^2 \left( \frac{E_p I_p}{2l_i} + \sum_{j=1}^3 \frac{E_s I_{s,j}}{2l_{i,j}} \right) \quad (10)$$

where  $E_p I_p$  and  $E_s I_{s,j}$  is the flexural rigidity of the primary and the  $j^{th}$  secondary backbone, respectively. The infinitesimal work done by the repulsive force field is contributed by the work of the respective forces  $\mathbf{f}_i$  on the  $i^{th}$  *psp*:

$$\delta W = \sum_i \mathbf{f}_i^T \delta \mathbf{p}_i = \sum_i \mathbf{f}_i^T \mathbf{J}_{v\tilde{\psi}}^{(i)} \delta \tilde{\psi} \quad (11)$$

where  $\mathbf{J}_{v\tilde{\psi}}^{(i)} \triangleq \frac{d\mathbf{p}_i}{d\tilde{\psi}}$  is the translational Jacobian of the  $i^{th}$  *psp*. Considering  $\delta\Pi = \frac{\partial\Pi}{\partial\tilde{\psi}} \delta\tilde{\psi}$ ,  $\delta U = \frac{dE}{d\tilde{\psi}} \delta\tilde{\psi}$  and Eq (11),

$$\nabla_{\tilde{\psi}} \Pi = \nabla_{\tilde{\psi}} E - \sum_i \mathbf{J}_{v\tilde{\psi}}^{(i)T} \mathbf{f}_i \quad (12)$$

Thus,

$$\Pi = E - \int \sum_i \mathbf{f}_i^T \mathbf{J}_{v\tilde{\psi}}^{(i)} d\tilde{\psi} \quad (13)$$

The derivation of  $\mathbf{J}_{v\tilde{\psi}}^{(i)}$  is straightforward given the Jacobian of each MBCR segment (see [25] for details).

<sup>3</sup>The problem of reaching local minima may happen that causes the motion planning to stop prematurely. Supplementing the potential method with well-tuned randomized best-first algorithms to escape local minima can solve this problem [23].

### B. Repulsive Force Field

A repulsive force field that can minimize image occlusion is characterized such that

- For a psp inside the cone, it increases at a rapid rate as the psp's distance to the cone face increases.
- For a psp outside the cone, it decreases as the psp's distance to the cone face increases.
- After a certain distance (distance of influence  $d_0$ ), outside the cone, it vanishes.
- The closer the psp is to the vertex of the cone, the more the endoscopic occlusion, hence the greater the force.

To formulate a force field with the above characteristics, we first define distance variables with respect to the FOV cone.

1) Conical Distance Parameters: Fig. 2-a shows an arbitrary point ( $\mathbf{psp}_i$ ) and the cone of FOV in its local frame ( $\{lens\}$ ). We define *canonical distance*  $d$  and *canonical slant height*  $r$  as shown in Fig. 2-a. Canonical distance  $d$  is measured from the surface of the FOV cone to the psp. The slant height  $r$  is measured from the origin of the FOV cone to a point on the cone surface that is closest to the psp. The distance  $d$  is defined as:

$$d = \begin{cases} > 0 & \text{if point is outside the cone} \\ < 0 & \text{if point is inside the cone} \\ = 0 & \text{if point is on the cone} \end{cases} \quad (14)$$

To determine  $(d, r)$  given  $\mathbf{psp}(x, y, z)$  and  $\beta$ , first, the position of  $\mathbf{psp}$  in  $\{lens\}$  is calculated using a homogeneous transformation

$${}^{lens}\mathbf{psp} \triangleq \begin{bmatrix} x_l \\ y_l \\ z_l \end{bmatrix} = {}^{lens}\mathbf{R}_w \mathbf{psp} + {}^{lens}\mathbf{p}_{org,w} \quad (15)$$

where  ${}^{lens}\mathbf{R}_w = e^{\alpha \hat{\mathbf{e}}_2} e^{-\gamma \hat{\mathbf{e}}_3}$  is the rotation transformation from  $\{w\}$  to  $\{lens\}$  and  ${}^{lens}\mathbf{p}_{org,w} = [0, -d_o, 0]^T$  is the position of the origin of  $\{w\}$  described in  $\{lens\}$  and  $d_o$  is the center-to-center distance of robot and endoscope channels (Fig. (1)-a).  $\gamma$  and  $\alpha$  is the angle of rotation of endoscope and lens inclination angle respectively.

It is straightforward to show by geometry that the canonical distance of  $\mathbf{psp}$  is:

$$d = \cos(\beta) \sqrt{x_l^2 + y_l^2} - \sin(\beta) z_l \quad (16)$$

where  $\beta$  is the half of the vertex angle of the cone (Fig. (2)-a)) and the canonical slant height is:

$$r = \sin(\beta) \sqrt{x_l^2 + y_l^2} + \cos(\beta) z_l \quad (17)$$

2) Repulsive Force Field: Denoting  $f^*$  as the nominal force magnitude on the cone face at nominal slant height  $r = r^*$ , we define the repulsive force as:

$$\mathbf{f}(d, r) = \begin{cases} \frac{f^*}{(r/r^*)^q} \left( \frac{d}{d_0} - 1 \right)^{2p} \hat{\mathbf{f}} & d/d_0 \leq 1, r \geq 0 \\ 0 & \text{otherwise} \end{cases} \quad (18)$$

$r^*$  and  $f^*$  as well as power variables  $p$  and  $q$  in the above equation help determine the magnitude and the growth of the

force field.  $\hat{\mathbf{f}}$  is the unit direction vector of the force that is  $\hat{\mathbf{f}} = {}^w\mathbf{R}_{lens} {}^{lens}\hat{\mathbf{f}}$  where

$${}^{lens}\hat{\mathbf{f}} = \left[ \frac{x_l \cos(\beta)}{\sqrt{x_l^2 + y_l^2}}, \frac{y_l \cos(\beta)}{\sqrt{x_l^2 + y_l^2}}, -\sin(\beta) \right]^T \quad (19)$$

Fig. 2-b shows the plot of the force magnitude for  $|d/d_0| \leq 1$ ,  $p = 1$ ,  $q = 2$  and multiple values of  $r/r^*$ .

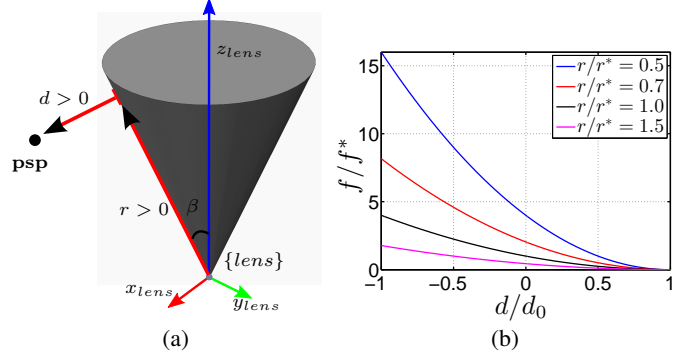


Fig. 2: (a) Conical distance parameters  $(r, d)$ , (b) Force field magnitude as a function of canonical distance

### C. Optimization Framework

The gradient descent method is adopted in order to minimize the potential function  $\Pi$ . This approach provides local minimization if certain conditions (convex function and Lipschitz gradient) are satisfied [26]. Therefore, the following  $\dot{\psi}$  minimizes  $\Pi$ :

$$\dot{\psi} = -\eta \nabla_{\tilde{\psi}} \Pi, \quad \eta > 0 \quad (20)$$

The problem in Eq. (9) can be cast as a quadratic programming problem (QP) where the main task of tracking the command velocity is treated as a constraint.

$$\begin{aligned} & \underset{\dot{\psi}}{\text{Minimize}} \quad \frac{1}{2} (\dot{\psi} + \eta \nabla_{\tilde{\psi}} \Pi)^T \mathbf{W}_1 (\dot{\psi} + \eta \nabla_{\tilde{\psi}} \Pi) \\ & \text{subject to} \quad \mathbf{J}_{x\tilde{\psi}} \dot{\psi} = \dot{\xi} \end{aligned} \quad (21)$$

where  $\mathbf{W}_1 \in \mathbb{R}^{7 \times 7}$  is a positive-definite weight matrix. The solution to this optimization problem that is also known as *Projected Gradient Method* ([22], [27]) is as follows

$$\dot{\psi}^* = \mathbf{J}_{x\tilde{\psi}}^\dagger \dot{\xi} - \eta (\mathbf{I}_7 - \mathbf{J}_{x\tilde{\psi}}^\dagger \mathbf{J}_{x\tilde{\psi}}) \nabla_{\tilde{\psi}} \Pi \quad (22)$$

where  $\mathbf{I}_7 \in \mathbb{R}^{7 \times 7}$  is the identity matrix,  $\nabla_{\tilde{\psi}} \Pi$  is substituted from Eq (12) and  $(\cdot)^\dagger$  represents the regularized weighted Moore-Penrose pseudo-inverse [28], [29]:

$$\mathbf{J}_{x\tilde{\psi}}^\dagger = \mathbf{W}_1^{-1} \mathbf{J}_{x\tilde{\psi}}^T (\mathbf{J}_{x\tilde{\psi}} \mathbf{W}_1^{-1} \mathbf{J}_{x\tilde{\psi}}^T + \epsilon \mathbf{I}_6)^{-1} \quad (23)$$

The regularizing term  $\epsilon \mathbf{I}_6$  serves to redefine matrix inversion to avoid singularities. If  $\epsilon$  is sufficiently small, this solution minimizes  $\Pi$  in the null-space of  $\mathbf{J}_{x\tilde{\psi}}$  i.e. the null-space projector  $\mathbf{I} - \mathbf{J}_{x\tilde{\psi}}^\dagger \mathbf{J}_{x\tilde{\psi}}$  projects the gradient vector  $\nabla_{\tilde{\psi}} \Pi$  in the null-space of the Jacobian, therefore it does not violate the constraint given by the pseudo-inverse solution [22].

To use the endoscope rotation angle  $\gamma$  to minimize the end effector-FOV center-to-center distance  $d_c$ , we choose:

$$\dot{\gamma}^* = -\eta \frac{\partial d_c}{\partial \gamma}, \quad \eta > 0 \quad (24)$$

$d_c$  can be shown by geometry to be

$$d_c = \sqrt{(x_l^2 + y_l^2 + z_l^2)} \sin(\beta + \mu) \quad (25)$$

where  $\mu = \text{atan}(d_{ee}/r_{ee})$ .  $r_{ee}, d_{ee}$  are the canonical distance parameters of the end effector.

#### D. Implementation

A resolved rate method is used to determine  $\dot{\xi}$  in Eq (22) in order to track the desired end-effector pose  $\xi_{des}$ , thus,

$$\begin{aligned} \dot{\xi} &= \begin{bmatrix} v_{des} \hat{e}_p \\ \omega_{des} \hat{e}_\zeta \end{bmatrix} \\ \hat{e}_p &= \frac{\mathbf{p}_{ee,des} - \mathbf{p}_{ee}}{\|\mathbf{p}_{ee,des} - \mathbf{p}_{ee}\|}, \\ \hat{e}_\zeta &= \text{Axis}(\mathbf{R}_{ee,des} \mathbf{R}_{ee}^T) \end{aligned} \quad (26)$$

where  $v_{des}, \omega_{des}$  are the desired end effector linear and rotational velocities,  $\mathbf{p}_{ee,des}, \mathbf{R}_{ee,des}, \mathbf{p}_{ee}, \mathbf{R}_{ee}$  is the desired and current end effector position and orientation respectively.  $\text{Axis}(\cdot)$  represents the axis of a rotation matrix in axis-angle orientation representation [22].

The Euler method is applied to solve Eq (22) and (24) to obtain  $\tilde{\psi}^*$  and  $\gamma^*$ . The steps to implement the algorithm are summarized in Algorithm (1).

#### Algorithm 1 Occlusion Minimization

**Input:**  $\Delta t, t_f, \tilde{\psi}_0, \gamma_0$   
**Output:**  $\tilde{\Psi} = [\psi_1, \psi_2, \dots]$ ,  
 $\gamma = [\gamma_1, \gamma_2, \dots]$   $\triangleright$  Solutions at each step  
1:  $\tilde{\psi} = \tilde{\psi}_0, \gamma = \gamma_0, \dot{\tilde{\psi}} = 0, \dot{\gamma} = 0, k = 0$   $\triangleright$  Initialization  
2: **while**  $k\Delta t \leq t_f$  **do**  
3:  $k \leftarrow k + 1$   
4:  $\tilde{\psi}_k = \tilde{\psi}_{k-1} + \dot{\tilde{\psi}}_{k-1} \Delta t$   $\triangleright$  Numerical integration  
5:  $\gamma_k = \gamma_{k-1} + \dot{\gamma}_{k-1} \Delta t$   $\triangleright$  Numerical integration  
6:  $\tilde{\psi}_{k-1} \leftarrow \mathbf{J}_{x\tilde{\psi}}^\dagger \dot{\xi} - \eta(\mathbf{I}_7 - \mathbf{J}_{x\tilde{\psi}}^\dagger \mathbf{J}_{x\tilde{\psi}}) \nabla_{\tilde{\psi}} \Pi$   $\triangleright$  Eq (2), (12), (23) and (26)  
7:  $\dot{\gamma}_{k-1} \leftarrow -\eta \frac{\partial d_c}{\partial \gamma}$   $\triangleright$  Eq (24), (25)  
8: **end while**

#### E. Visual Occlusion Index (VOI)

In order to compare the visual occlusion in different scenarios, a measure called *visual occlusion index (VOI)* is introduced. This measure is the ratio of the volume of the approximated occluded frustum to the volume of the cone of FOV whose base is at the end-effector tip. Figure (3a) illustrates a planar schematic of the approximate frustum of occlusion (hatched area) induced by an MBCR.  $\nu$  is the maximum subtended angle of the MBCR structure from the point of entry into the cone.  $r_e$  and  $r_{max}$  is the canonical slant height of the entry point and the end effector respectively. As such,  $VOI$  can be shown to be

$$VOI = \frac{(1 + \cot^2(\beta))^2 \tan^2(\nu)}{4(\cot(\beta) + \tan(\nu))^2} \left(1 - \left(\frac{r_e}{r_{max}}\right)^3\right) \quad (27)$$

where  $\nu$  is saturated at  $2\beta$ , i.e. in situations where the MBCR passes across the cone,  $\nu = 2\beta$ .

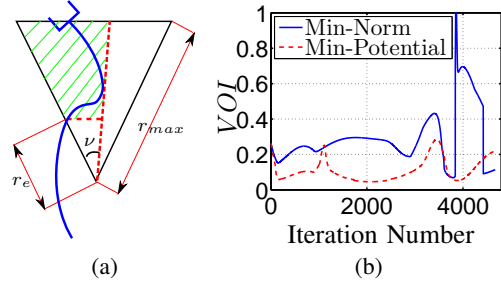


Fig. 3: (a) Illustration of occlusion frustum (hatched area), (b) Visual occlusion index in tracking a circle

## V. RESULTS & DISCUSSIONS

To validate the proposed method, several simulations were performed in MATLAB® environment. Table I summarizes the parameters values used in the simulations.

TABLE I: Simulation parameters

Param.	Value	Param.	Value	Param.	Value
$\Delta t$	1ms	$\eta_1$	30	$\eta_2$	30
$\epsilon$	$10^{-6}$	$d_o$	4.47mm	$\alpha$	$30^\circ$
$\beta$	$27.5^\circ$	$d_0$	5mm	$r^*$	60mm
$f^*$	5N	$l_i$	{26, 20, 19}mm	$r_{disk}$	2.5mm

psp's were situated as follows.  $\frac{s_{1,L}}{l_1} = [0.5, 0.75, 1]$ ,  $\frac{s_{2,L}}{l_2} = [0.25, 0.5, 0.75, 1]$  and  $\frac{s_{3,L}}{l_3} = [0.25, 0.50, 0.75]$  where  $s_{j,L}$  denotes the arc distances of psp's on the  $j^{th}$  segment. The locations were chosen by heuristics and also by inspection of simulation results.

The first task is to maintain the end effector pose with  $\gamma = 0$  to examine the performance of the algorithm presented in algorithm (1). This simulation also helps select the locations and the number of psp's and to tune other parameters such as  $\eta_1$  so as to elicit the desired behavior in converging to the equilibrium. Fig. (4) and the multimedia extension show the MBCR at the start and the end of simulation. The forces are shown by blue vectors and the base translation motion is represented by a magenta trail. The plots in Fig. (5a) and (5b) shows the potential energy and the VOI in the same simulation respectively.

At iteration  $\approx 800(0.8secs)$ , the MBCR is pushed outside the cone into the static equilibrium enforced by the imparting forces and the energy of the MBCR (Eq (10)) while the tip remains stationary. The VOI converges to 0.16 from initial value of 0.25.

A second task is to track a circle of radius 10mm while orienting the end effector central axis (blue axis at the tip) along the normal to the circle plane ( $\hat{n}$  in Fig. (6)). The center of the circle is fixed on the axis of the FOV cone at  $t = 0$ . To minimize  $d_c$  while the tip is tracking the circle, the endoscope rotates from  $0^\circ$  to  $-23.7^\circ$  and then goes to  $25.1^\circ$  and ends up close to  $0^\circ$  for a full circle tracking. The top snapshots in Fig. (6) demonstrate how the



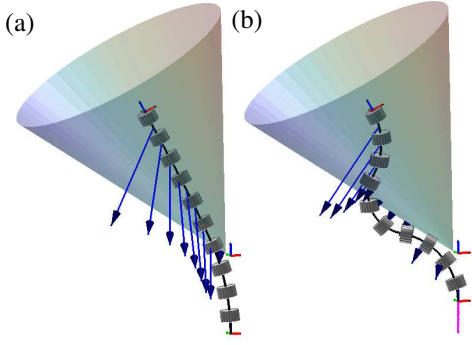


Fig. 4: Maintaining end effector pose and converging to a minimal-occlusion posture (a) Initial posture, (b) Final Posture, Note there is no endoscope rotation.

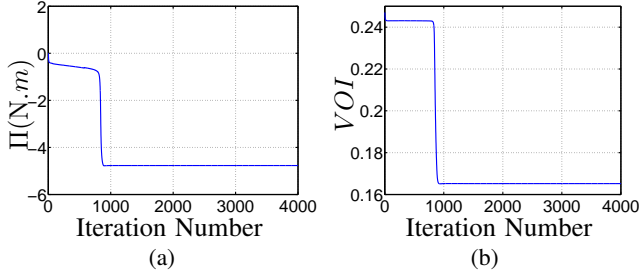


Fig. 5: Min-potential solution for the task of maintaining end effector pose: (a) Potential energy, (b) Visual occlusion index

robot accomplished this task using a minimum-norm solution (pseudo-inverse). The bottom snapshots show the same task at the same instants accomplished by using minimum-potential solution in Eq (22). As it can be seen in the top pictures, most of the MBCR body is inside the FOV (or just outside of it). This is explained by the fact that a pseudo-inverse solution minimizes the configuration space change from the initial configuration (top left picture) to achieve the task. Examining the bottom pictures shows that the robot achieves the task of tracking by using the configurations that are generally leaning outside the FOV hence not obstructing the camera visual. Both these simulations are shown in the multimedia extension.

The plots of Fig. (3b) show the VOI for the two solutions. The average VOI for the minimum-potential and the minimum-norm solution are 0.11 and 0.29 respectively confirming the efficacy of the minimum-potential solution. At iteration 3840, the VOI of the minimum-norm solution jumps from 0.08 to 1 and then starts falling back down at iteration 3864. During this period, the first segment enters the FOV and obstructs it very close to the cone vertex ( $r = 2.3mm$  at iteration 3841) and then leaves it.

The choice of number and location of psp's affects the solution of the redundancy method and the computational cost. For instance, in our simulations, it was observed that using  $\frac{s_{1,L}}{l_1} = [0.5 : 0.05 : 1]$ ,  $\frac{s_{2,L}}{l_2} = [0.25 : 0.05 : 1]$  and  $\frac{s_{3,L}}{l_3} = [0.25 : 0.05 : 0.75]$  caused the MBCR to be pushed further outward since more psp's increase the resultant forces. In our opinion, infinite number of points distributed evenly across the body of a planar MBCR (or a continuously

distributed force) generates the globally minimal occlusion. However, apart from computational considerations, this may not be true for a general spatial continuum robot and requires more investigation. Although psp's selection was performed heuristically in our simulations, other approaches are worth investigating. For instance, it is possible to use *floating* psp's such that at each iteration of the algorithm, the closest point to the cone per segment is assigned as a psp.

Note that it is also possible to affect the equilibrium configuration and the rate of convergence by adjusting the force magnitudes in Eq (18). Whether the same behavior can be achieved by changing the number of psp's remains to be investigated. Regardless, a caveat is that too many psp's or excessively large force magnitudes may cause excessive null-space motion that can intervene with the main task depending on the value of  $\epsilon$ . Moreover, the time step  $\Delta t$ ,  $\eta_1$  and  $\eta_2$  are important parameters too. Note that the gradient descent step size is ultimately determined by  $\eta_1 \cdot \Delta t$  (or  $\eta_2 \cdot \Delta t$ ).

The parameter  $\epsilon$  in Eq (22) requires careful tuning. if it's too small (typically less than  $10^{-6}$  in our simulations), the MBCR assumes extremely large configuration rates and loses tracking when it's close to singular configuration ( $\theta_{iL} = \pi/2$ ). If it's too large (typically greater than  $10^{-4}$  in our simulations), the main tracking task is jeopardized as the null-space solution loses its validity thus interfering with the tracking task.

## VI. CONCLUSIONS

In this paper, a redundancy resolution method was developed to minimize the visual field occlusion caused by the presence of the robot in the field of view(FOV). The method is based on a modified artificial potential field that drives the robot outside the FOV in attempting to reach static equilibrium while achieving the main task of tracking. Simulations for the tasks of maintaining the end effector pose and tracking a circle confirmed the efficacy of the proposed method for a rotating camera. Although the proposed method was developed within the context of multi-backbone continuum robots, it can be generally applied to any redundant robot that requires to stay as clear of the visual field as possible, whether the redundancy is inherent to the robot (e.g. 7-DoF robot) or it is with respect to the task (e.g. Cartesian position tracking by a 6-DoF robot). Experimental evaluation of the proposed method with a moving camera is currently in progress.

## ACKNOWLEDGMENT

The authors would like to thank Rashid Yasin and Long Wang for their valuable comments.

## REFERENCES

- [1] R. E. Goldman, A. Bajo, L. S. MacLachlan, R. Pickens, S. D. Herrell, and N. Simaan, "Design and Performance Evaluation of a Minimally Invasive Telerobotic Platform for Transurethral Surveillance and Intervention," *IEEE Transactions on Biomedical Engineering*, vol. 60, no. 4, pp. 918–925, Apr. 2013.
- [2] R. B. Pickens, A. Bajo, N. Simaan, and D. Herrell, "A Pilot Ex Vivo Evaluation of a Telerobotic System for Transurethral Intervention and Surveillance," *Journal of Endourology*, vol. 29, pp. 231–234, 2015.

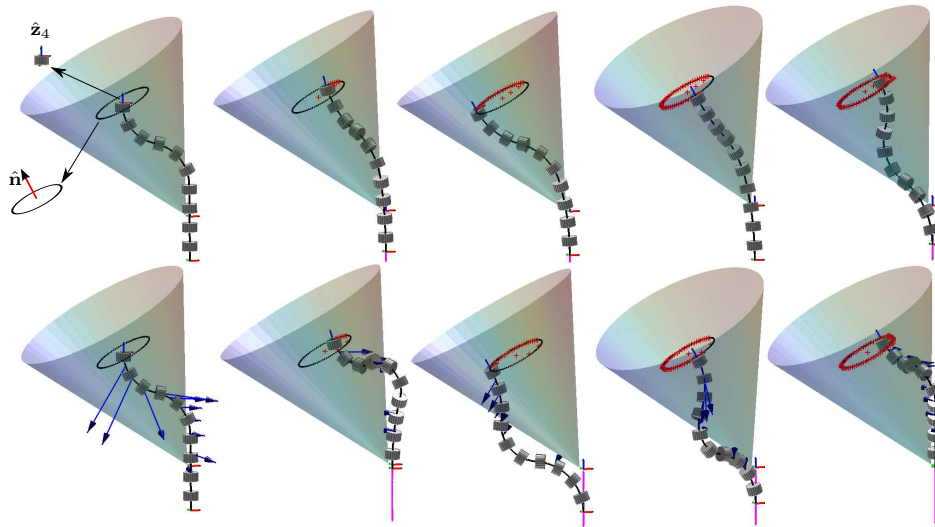


Fig. 6: Application of Algorithm (1) for the main task of tracking a  $\varnothing 20\text{mm}$  circle while keeping end effector's  $\hat{z}_4$  axis along the normal to the circle plane  $\hat{n}$ . Top and bottom rows display min-norm and min-potential solutions respectively. Note endoscope rotation as observed by change in the orientation of the cone of field of view.

- [3] N. Sarli, G. Del Giudice, S. Herrell, D., and N. Simaan, "A resectoscope for robot-assisted transurethral surgery," *ASME Journal of Medical Devices*, in press.
- [4] A. T. Hillel, A. Kapoor, N. Simaan, R. H. Taylor, and P. Flint, "Applications of robotics for laryngeal surgery," *Otolaryngologic Clinics of North America*, vol. 41, no. 4, pp. 781–791, 2008.
- [5] J. Li and J. Xiao, "Task-constrained continuum manipulation in cluttered space," in *2014 IEEE International Conference on Robotics and Automation (ICRA)*, May 2014, pp. 2183–2188.
- [6] A. Reiter and P. K. Allen, "An online learning approach to in-vivo tracking using synergistic features," in *Intelligent Robots and Systems (IROS), 2010 IEEE/RSJ International Conference on*. IEEE, 2010, pp. 3441–3446.
- [7] L. E. Kavraki, P. Svestka, J. C. Latombe, and M. H. Overmars, "Probabilistic roadmaps for path planning in high-dimensional configuration spaces," *IEEE Transactions on Robotics and Automation*, vol. 12, no. 4, pp. 566–580, 1996.
- [8] M. A. Baumann, D. C. Dupuis, S. Leonard, E. A. Croft, and J. J. Little, "Occlusion-free path planning with a probabilistic roadmap," *2008 IEEE/RSJ International Conference on Intelligent Robots and Systems, IROS*, pp. 2151–2156, 2008.
- [9] M. Baumann, S. Leonard, E. A. Croft, and J. J. Little, "Path planning for improved visibility using a probabilistic road map," *IEEE Transactions on Robotics*, vol. 26, no. 1, pp. 195–200, 2010.
- [10] S. Leonard, E. A. Croft, and J. J. Little, "Planning collision-free and occlusion-free paths for industrial manipulators with eye-to-hand configuration," *2009 IEEE/RSJ International Conference on Intelligent Robots and Systems, IROS 2009*, pp. 5083–5088, 2009.
- [11] G. Morel, T. Liebezeit, J. Szweczyk, S. Boudet, and J. Pot, "Explicit incorporation of 2D constraints in vision based control of robot manipulators," in *Experimental Robotics VI*. London: Springer London, 2000, pp. 99–108.
- [12] P. Corke and S. Hutchinson, "A new partitioned approach to image-based visual servo control," *IEEE Transactions on Robotics and Automation*, vol. 17, no. 4, pp. 507–515, 2001.
- [13] Y. Mezouar and F. Chaumette, "Avoiding self-occlusions and preserving visibility by path planning in the image," *Robotics and Autonomous Systems*, vol. 41, no. 2, pp. 77–87, 2002.
- [14] N. Cowan, "Binocular visual servoing with a limited field of view," in *In Mathematical Theory of Networks and Systems, Notre*, 2002.
- [15] V. Lippiello, B. Siciliano, and L. Villani, "An Occlusion Prediction Algorithm for Visual Servoing Tasks in a Multi-Arm Robotic Cell," in *2005 International Symposium on Computational Intelligence in Robotics and Automation*. IEEE, 2005, pp. 733–738.
- [16] N. Simaan, R. H. Taylor, and P. Flint, "A Dexterous System for Laryngeal Surgery," in *2004 IEEE International Conference on Robotics and Automation*. New Orleans, LA: IEEE, 2004, pp. 351–357.
- [17] N. Simaan, K. Kai Xu, W. Wei Wei, A. Kapoor, P. Kazanzides, R. Taylor, and P. Flint, "Design and Integration of a Telerobotic System for Minimally Invasive Surgery of the Throat," *The International Journal of Robotics Research*, vol. 28, no. 9, pp. 1134–1153, sep 2009.
- [18] R. E. Goldman, A. Bajo, and N. Simaan, "Compliant motion control for multisegment continuum robots with actuation force sensing," *IEEE Transactions on Robotics*, vol. 30, no. 4, pp. 890–902, 2014.
- [19] A. Bajo, R. B. Pickens, S. D. Herrell, and N. Simaan, "Constrained motion control of multisegment continuum robots for transurethral bladder resection and surveillance," in *Proceedings - IEEE International Conference on Robotics and Automation*, 2013, pp. 5837–5842.
- [20] A. A. Maciejewski and C. A. Klein, "Obstacle avoidance for kinematically redundant manipulators in dynamically varying environments," *The international journal of robotics research*, vol. 4, no. 3, pp. 109–117, 1985.
- [21] O. Khatib, "Real-Time Obstacle Avoidance for Manipulators and Mobile Robots," *The International Journal of Robotics Research*, vol. 5, no. 1, pp. 90–98, 1986.
- [22] B. Siciliano, L. Sciacivico, L. Villani, and G. Oriolo, *Robotics: Modelling, Planning and Control*, 1st ed. Springer Publishing Company, Incorporated, 2008.
- [23] J.-C. Latombe, *Robot motion planning*. Kluwer Academic Publishers, 1991.
- [24] K. Xu and N. Simaan, "An investigation of the intrinsic force sensing capabilities of continuum robots," *IEEE Transactions on Robotics*, vol. 24, no. 3, pp. 576–587, 2008.
- [25] A. Bajo and N. Simaan, "Kinematics-based detection and localization of contacts along multisegment continuum robots," *IEEE Transactions on Robotics*, vol. 28, no. 2, pp. 291–302, April 2012.
- [26] S. Boyd and L. Vandenberghe, *Convex Optimization*. New York, NY, USA: Cambridge University Press, 2004.
- [27] A. Liegeois, "Automatic Supervisory Control of the Configuration and Behavior of Multibody Mechanisms," *IEEE Transactions on Systems, Man, and Cybernetics*, vol. 7, no. 12, pp. 868–871, 1977.
- [28] E. H. Moore, "On the reciprocal of general algebraic matrix," *Bulletin of the American Mathematical Society*, vol. 26, no. 9, pp. 394–395, 1920.
- [29] P. Lancaster and M. Tismenetsky, *The Theory of Matrices with Applications*, 2nd ed. Academic Press, 1985.